Inorganica Chimica Acta 477 (2018) 257–269

Contents lists available at ScienceDirect

Inorganica Chimica Acta

journal homepage: www.elsevier.com/locate/ica

Research paper

Coordination susceptibilities of cinnamaldehyde and cuminaldehyde derived Schiff bases towards the *fac*-$[Re(CO)_3]^+$ core: Formation, computational and DNA interaction studies

Muhammed Bilaal Ismail, Irvin Noel Booysen *, Matthew Piers Akerman

School of Chemistry and Physics, University of KwaZulu-Natal, Private Bag X01, Scottsville 3209, Pietermaritzburg, South Africa

ARTICLE INFO

Article history:
Received 24 January 2018
Received in revised form 15 March 2018
Accepted 16 March 2018
Available online 27 March 2018

Keywords:
Rhenium
Schiff base
DNA interaction
Molecular docking
Gel electrophoresis

ABSTRACT

Herein, we explore the coordination behaviours of Schiff bases derived from constituents of essential oils (*viz.* cinnamaldehyde and cuminaldehyde) and aromatic amines (*viz.* 2-aminophenol and 4-aminoantipyrene) towards the *facial* tricarbonylrhenium(I) core. The resultant rhenium(I) compounds: $(\mu\text{-X})_2[Re(CO)_3]_2$ {where X = 2-{[3-phenylprop-2-en-1-ylidene]amino}phenol (ciap) (for **1**) or 2-{[4-(propan-2-yl)benzylidene]amino}phenol (cuap) (for **2**), *fac*-$[Re(CO)_3(apy)Cl]$ (apy = 4-aminoantipyrene) (**3**) and *fac*-$[Re(CO)_3(cinap)Cl]$ (cinap = 1, 5-dimethyl-2-phenyl-4-{[3-phenylprop-2-en-1-ylidene]amino}-1,2-dihydro-3*H*-pyrazol-3-one) (**4**) were formed. The metal compounds were spectroscopically characterized and structural elucidations were confirmed by single crystal X-ray diffraction. DFT studies were utilized to rationalize the contrasting coordination behaviours of the structural analogues, 1,5-dimethyl-2-phenyl-4-{[4-(propan-2-yl)benzylidene]amino}-1,2-dihydro-3*H*-pyrazol-3-one (cumap) and cinap in the formation of **3** and **4**, respectively. These metal compounds showed affinities towards Calf-Thymus DNA based on UV-Vis DNA binding titrations and molecular docking studies revealed that they are groove binders. In addition, gel electrophoresis experiments indicated that steric factors has an influence on the DNA cleavage activities of the mono- and dinuclear rhenium(I) compounds.

1. Introduction

Essential oils are natural, pungent and volatile compounds which are formed by plants as secondary metabolites. They are extracted from various florae originating from temperate and tropical countries where they represent an important part of the traditional pharmacopoeia [1]. In this study, constituents of essential oils, cinnamaldehyde and cuminaldehyde Fig. 1, have been utilized partly due to their inherent biological activities [2,3]. Under i*n vivo* experimental conditions, cinnamaldehyde has shown to decrease plasma glucose, glycosylated haemoglobin, cholesterol and increase insulin levels while similar traits are observed for cuminaldehyde with hypoglycaemic effects being in the majority [4]. Moreover, both organic compounds have revealed anti-inflammatory and anticancer properties [5–8]. Such complementary properties may allow these natural occurring compounds and their derivatives to form chemotherapeutic compounds which minimize the traditional side-effects of current anticancer agents.

Metal complexes of cinnamaldehyde and cuminaldehyde are scarcely found in literature possibly because they lack electron-donating atoms in order to form metal-stabilizing bidentate or tridentate ligands. However, these bio-aldehydes can become extended *pi*-aromatic systems by the formation of Schiff bases. An example thereof is *N, N′–bis*(α-methyl-*trans*-cinnamadehyde) ethylenediimine (L) which was isolated from the 1:2 M condensation reaction between α-methyl-*trans*-cinnamaldehyde and ethylenediamine. This diimine, L, afforded metal(II) complexes with general formula of $[ML_2Cl_2]$ (where M = Ni or Co) which displayed high anticandidal activity accompanied with limited toxicity towards vertebrate cells [9]. Additionally, biologically relevant Schiff bases derived from thiosemicarbazone with *trans*-cinnamaldehyde (Htcin) and cuminaldehyde (Htcum) coordinate as bidentate monoanionic chelates to nickel(II) and copper(II) centres; *viz.* $[Ni(X)_2]\cdot H_2O$ and $[Cu(X)(H_2O)Cl]$ where X = tcin or tcum. These transition metal complexes exhibit properties which are practical for in vivo antileukemic exploration [10].

In this research study, two dinuclear *facial* tricarbonylrhenium (I) compounds were isolated from a "one-pot" synthetic method of equimolar ratios (1:1:1 stoichiometry) featuring chloropentacarbonylrhenium(I), 2-aminophenol and one of the relevant

* Corresponding author.
E-mail address: Booyseni@ukzn.ac.za (I.N. Booysen).

https://doi.org/10.1016/j.ica.2018.03.032
0020-1693/

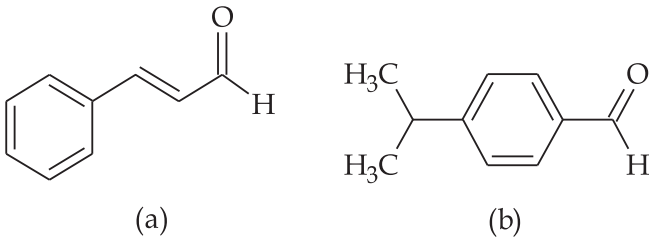

Fig. 1. Structures of cinnamaldehyde (a) and cuminaldehyde (b).

natural oils, cinnamaldehyde or cuminaldehyde to afford $(\mu\text{-X})_2[Re(CO)_3]_2$ {where X = 2-{[3-phenylprop-2-en-1-ylidene]amino}phenol (ciap) (for **1**) or 2-{[4-(propan-2-yl)benzylidene]amino}phenol (cuap) (for **2**)} Scheme 1. Mononuclear rhenium(I) complexes, *fac*-$[Re(CO)_3(apy)Cl]$ (apy = 4-aminoantipyrene) (**3**) and *fac*-$[Re(CO)_3(cinap)Cl]$ (cinap = 1, 5-dimethyl-2-phenyl-4-{[3-phenylprop-2-en-1-ylidene]amino}-1,2-dihydro-3*H*-pyrazol-3-one) (**4**) were formed from exploring the coordination behaviours of the Schiff bases derived from the respective natural oils and 4-aminoantipyrene Scheme 2. The structural elucidations were confirmed by single crystal X-ray diffraction and supported by spectroscopic characterization. Interestingly for **3**, its solid-state structure showed that cumap underwent hydrolysis and as a result only the apy moiety coordinated to the *fac*-$[Re(CO)_3Cl]$ unit as opposed to **4** where the cinap Schiff base moiety remained intact. The contrasting coordination behaviours of the aforementioned structural analogues, cumap and cinap were rationalized using computational studies at the DFT level. Furthermore, biological interaction studies of **1**–**4** were conducted in the form of CT-DNA titrations, gel electrophoresis and supported by molecular docking simulations.

2. Experimental

2.1. Materials and methods

Rhenium pentacarbonyl chloride, electrochemical grade tetrabutylammoniumtetrafluoroborate, 2-aminophenol, 4-aminoantipyerene, cinnamaldehyde, cuminaldehyde, phosphate buffered saline (PBS) tablets and calf thymus (CT) DNA were obtained from Sigma Aldrich. DNA chips, DNA 1 K gel and stain, DNA ladder and loading buffer were all obtained within a DNA 1 K Analysis Kit from Bio-Rad. All solvents were obtained from Merck SA. These chemicals were used without any further purification. The infrared spectra were recorded on a Perkin–Elmer Spectrum 100 from 4000 to 650 cm^{-1}. ^1H NMR spectra were obtained using a Bruker Avance 400 MHz spectrometer. All NMR spectra were recorded in DMSO-d_6. UV-Vis spectra were recorded using a Perkin-Elmer Lambda 25. Melting points were determined using a Stuart SMP3 melting point apparatus. The conductivity measurements were determined at 295 K on a Radiometer R21M127 CDM 230 conductivity and pH meter. Toluene was dried with sodium wire and stored in the presence of dry 4 Å microsieves. The redox properties of the metal complexes were investigated by cyclic and square wave voltammetry. The concentration of the metal complexes was 2 mM and tetrabutylammoniumtetrafluoroborate (0.1 M) was used as the supporting electrolyte. A Metrohm Autolab Potentiometer was used for measurements equipped with a three electrode system: pseudo Ag|AgCl reference electrode, a glassy carbon working electrode (GCE) and Pt auxiliary counter electrode.

2.2. 1,5-Dimethyl-2-phenyl-4-{[4-(propan-2-yl)benzylidene]amino}-1,2-dihydro-3H-pyrazol-3-one (cumap)

Equimolar amounts of 4-aminoantipyrene (0.25 g; 1.23 mmol) and cuminaldehyde (0.87 cm^3; 1.23 mmol) were added to methanol (10 cm^3) and heated at a reflux for 3 h. Thereafter, the light orange solution was concentrated to an oily residue. Upon cooling to room temperature, the substance precipitated. Afterwards, 15 cm^3 of petroleum ether was added to the precipitate and the resultant mixture was stirred for an hour. Then a cream-coloured precipitate was filtered, washed with cold methanol (3 cm^3) and hexane (3 cm^3), then allowed to dry in a desiccator. Yield = 68%; M.P. 191–196 °C; IR (ν_{max}/cm^{-1}): ν(C=O) 1654 (s), ν(C=N) 1595 (s), ν(C=C) 1447 (m). ^1H NMR (295 K/ppm, see Fig. 2): 9.57 (s, 1H, *H1*), 7.74 (d, 2H, *H14, H18*), 7.54 (t, 2H, *H15, H17*), 7.42–7.32 (m, 5H, *H3, H4, H9, H10, H16*), 3.18 (s, 3H, *H19, H19′, H19″*), 2.95 (m, 1H, *H6*), 2.46 (s, 3H, *H20, H20′, H20″*), 1.24 (d, 6H, *H7, H7′, H7″, H8, H8′, H8″*). UV–Vis (DCM, λ_{max} (ε, $M^{-1}\,cm^{-1}$)): 332 nm (48,374).

2.3. 1,5-Dimethyl-2-phenyl-4-{[3-phenylprop-2-en-1-ylidene]amino}-1,2-dihydro-3H-pyrazol-3-one (cinap)

Using the same experimental procedure as described in Section 2.2, the 1:1 M condensation reaction of 4-aminoantipyrene (0.25 g; 1.23 mmol) with cinnamaldehyde (0.16 cm^3; 1.23 mmol) was conducted methanol (10 cm^3) which resulted in the isolation of a deep orange precipitate. Yield = 63%; M.P. 188–192 °C; IR (ν_{max}/cm^{-1}): ν(C=O) 1637 (s), ν(C=N) 1570 (s), ν(C=C) 1524 (m). ^1H NMR (295 K/ppm): 9.42 (d, 1H, *H12*), 7.64 (d, 2H, *H2, H6*), 7.54 (t, 2H, *H3, H5*), 7.44–7.31 (m, 6H, *H13, H14, H16, H20, H17, H19*), 7.15–6.98 (m, 2H, *H18, H4*), 3.18 (s, 3H, *H11, H11′, H11″*), 2.41 (s, 3H, *H10, H10′, H10″*). UV-Vis (DCM, λ_{max} (ε, $M^{-1}\,cm^{-1}$)): 367 nm (38,980).

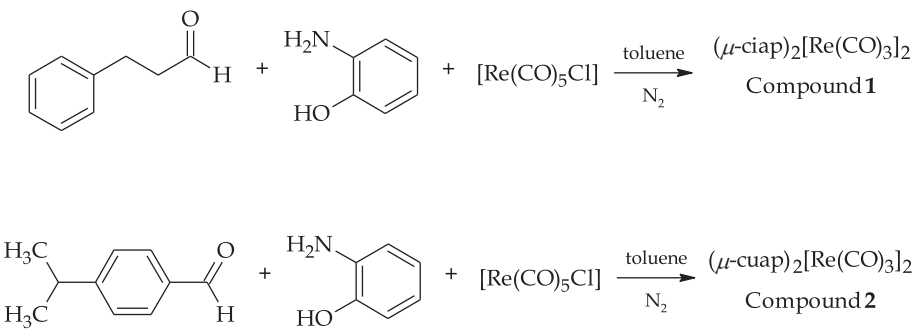

Scheme 1. Synthesis of the dinuclear rhenium(I) compounds **1** and **2**.

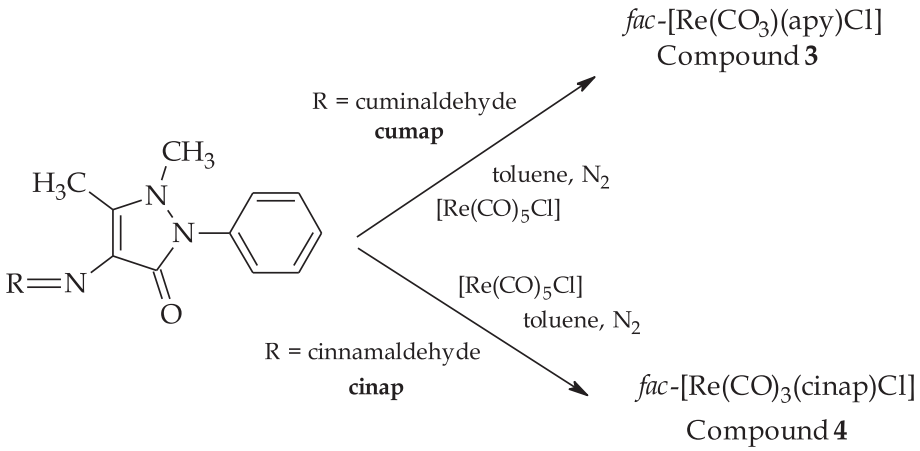

Scheme 2. Synthesis of the mononuclear rhenium(I) complexes **3** and **4**.

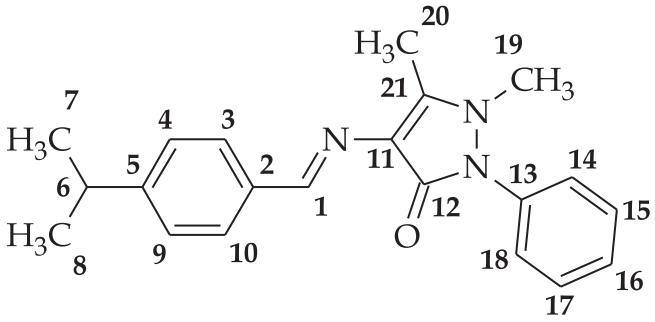

Fig. 2. The atomic numbering scheme of cumap.

2.4. (μ-*ciap*)$_2$[Re(CO)$_3$]$_2$ (1)

A 1:1 stoichiometric ratio of cinnamaldehyde (0.05 cm^3; 415 μmol) and 2-aminophenol (45.2 mg; 415 μmol) was added to toluene (20 cm^3) and heated to reflux for 5 h. To the cooled solution, a molar equivalent of [Re(CO)$_5$Cl] (150 mg; 415 μmol) was added and the reaction mixture was heated to reflux for a further 3 h under an inert N_2 atmosphere. Thereafter, the cooled solution was layered with *n*-hexane and after progressive slow diffusion, orange crystals suitable for X-ray analysis were collected. Yield = 24%; M.P. > 350 °C; Conductivity (DMF, 10^{-3} M) = 22.04 Ω^{-1}cm^{-2}-mol^{-1}; IR (υ_{max}/cm^{-1}): υ(C≡O)$_{fac}$ 2018 and 1874 (s), υ(C=N) 1610 (m), υ(C=C) 1565 (m); ^{1}H NMR (CDCl$_3$, 295 K/ppm): 8.52 (d, 2H, *H7, H7′*), 7.65–7.57 (m, 4H, *H2, H2′, H5, H5′*), 7.50–7.38 (m, 8H, *H3, H3′, H4, H4′, H8, H8′, H9, H9′*), 7.23 (d, 2H, *H11, H11′*), 7.24–7.15 (m, 4H, *H12, H12′, H13, H13′*), 7.02 (d, 2H, *H15, H15′*), 6.91 (t, 2H, *H14, H14′*); UV-Vis (MeOH, λ_{max} (ε, M^{-1} cm^{-1})): 283 nm (23,501); 306 nm (21,822); 345 nm (17,068), 461 nm (7396).

2.5. (μ-*(cuap)*$_2$[Re(CO)$_3$] (2)

The same experimental procedure was adopted as in Section 2.4, the following reagents were utilized: cuminaldehyde (0.06 cm^3; 415 μmol), 2-aminphenol (45.2 mg; 415 μmol) and [Re(CO)$_5$Cl] (150 mg; 415 μmol). Bright yellow, parallelogram-shaped crystals were isolated. Yield = 32%; M.P. > 350 °C; Conductivity (DMF, 10^{-3} M) = 20.95 Ω^{-1}cm^{-2}mol^{-1}; IR (υ_{max}/cm^{-1}): υ(C≡O)$_{fac}$ 2022 and 1882 (s), υ(C=N) 1686 (m), υ (C=C) 1610 (s); ^{1}H NMR (295 K/ppm): 8.71 (s, 2H, *H7, H7′*), 7.88 (d, 2H, *H1, H1′*), 7.85 (d, 2H, *H4, H4′*), 7.42 (d, 2H, *H9, H9′*), 7.38 (d, 2H, *H11, H11′*), 7.32 (d, 2H, *H10, H10′*), 7.21 (t, 2H, H5, H5′), 7.04 (d, 2H, *H13, H13′*), 6.93 (t, 2H, *H6, H6′*), 3.51 (s, 2H, *H14, H14′*), 2.88 (s, 6H, *H15A, H15B, H15C, H15A′, H15B′, H15C′*), 1.60 (s, 6H, *H16A, H16B, H16C, H16A′, H16B′, H16C′*); UV-Vis (MeOH, λ_{max} (ε, M^{-1}cm^{-1})): 282 nm (11810); 338 nm (5793); 390 nm (5081).

2.6. *fac*-[Re(CO)$_3$(apy)Cl] (3)

The 1:1 M coordination reaction of cumap (92.2 mg; 276 μmol) with [Re(CO)$_5$Cl] (100 mg; 276 μmol) were done in toluene (20 cm^3). The reaction mixture was heated until reflux for 4 h under inert conditions. The resultant solution was cooled in ice bath followed by filtration of a brown precipitate. This precipitate was washed with diethyl ether (3 cm^3) and allowed to dry in a desiccator. Then, the precipitate was dissolved in tetrahydrofuran and layered with *n*-hexane to afford rectangular crystals after 3 days. Yield = 31%; M.P. > 350 °C; Conductivity (DMF, 10^{-3} M) = 12.22 Ω^{-1} cm^{-2} mol^{-1}; IR (ν_{max}/cm^{-1}): υ(N—H) 3112 w; υ(C≡O)$_{fac}$ 2019 and 1872; υ(C=O) 1608 m; ^{1}H NMR (295 K/ppm): 7.68–7.62 (m, 2H, *H11, H13*), 7.58 (t, 1H, *H12*), 7.46–7.41 (m, 2H, *H10, H14*), 6.55 (d, 1H, *N1-H1A*), 5.65 (d, 1H, *N1-H1B*), 2.43 (s, 3H, *H8A, H8B, H8C*), 2.10 (s, 3H, *H7A, H7B, H7C*); UV-Vis (MeOH, λ_{max} (ε, M^{-1}cm^{-1})): 258 nm (46,274); 276 nm (38,815); 329 nm (9222).

2.7. *fac*-[Re(CO)$_3$(cinap)Cl] (4)

A solution of cinap (87.8 mg; 276 μmol) and [Re(CO)$_5$Cl] (100 mg; 276 μmol) in toluene (20 cm^3) was stirred at reflux temperature under N_2 for 4 h. The resultant reaction mixture was allowed to cool to room temperature. Then several aliquots of the reaction mixture were layered with *n*-hexane. After six days of slow diffusion of hexane into the reaction mixture, X-ray quality crystals were obtained. Yield = 22%; M.P. > 350 °C; Conductivity (DMF, 10^{-3} M) = 14.55 Ω^{-1} cm^{-2} mol^{-1}; IR (νmax/cm^{-1}): υ(C≡O)$_{fac}$ 2012 and 1888 s; υ(C=O) 1600 m; υ(C=N) 1584 m; ^{1}H NMR (295 K/ppm): 8.71 (d, 1H, *H12*), 7.82 (d, 1H, *H2*), 7.72–7.62 (m, 5H, *H6, H5, H3, H13, H14*), 7.58–7.48 (m, 6H, *H4, H16, H17, H18, H19, H20*), 3.47 (s, 3H, *H11A, H11B, H11C*), 2.76 (s, 3H, *H10A, H10B, H10C*); UV-Vis (MeOH, λ_{max} (ε, M^{-1} cm^{-1})): 235 nm (3675); 241 nm (3347); 288 nm (3597); 350 nm (4681).

2.8. X-ray crystallography

The X-ray data for **1–4** were recorded on a Bruker Apex Duo equipped with an Oxford Instruments Cryojet operating at 100 K and an Incoatec microsource operating at 30 W power. Crystal and structure refinement data for **3** and **4** are given in Table 1 while

their selected bond lengths and angles are given in Tables 2 and 3, respectively. Only low resolution structures could be attained for the dinuclear compounds **1** and **2**, see Figs. S10 and S11. The data was collected with Mo Kα (λ = 0.71073 Å) radiation at a crystal-to-detector distance of 50 mm. The following conditions were used for the Bruker data collection: omega and phi scans with exposures taken at 30 W X-ray power and 0.50° frame widths using APEX2 [11]. The data were reduced with the programme SAINT [11] using outlier rejection, scan speed scaling, as well as standard Lorentz and polarisation correction factors. A SADABS [11] semi-empirical multi-scan absorption correction was applied to the data [12]. Direct methods, SHELXS-97 [13] and WinGX [14] were used to solve the structure. All non-hydrogen atoms were located in the difference density map and refined anisotropically with SHELXL-97 [13]. All hydrogen atoms were included as idealised contributors in the least squares process. Their positions were calculated using a standard riding model with C-$H_{aromatic}$ distances of 0.93 Å and U_{iso} = 1.2 U_{eq}.

Table 1
Crystal data and structure refinement data for **3**·C_4H_8O and **4**·CH_2Cl_2.

	3·C_4H_8O	**4**·CH_2Cl_2
Chemical formula	$C_{18}H_{21}ClN_3O_5Re$	$C_{25}H_{23}Cl_5N_3O_4Re$
Formula weight	581.03	792.91
Temperature(K)	100(2)	100(2)
Crystal system	Monoclinic	Triclinic
Space group	$P2_1/c$	P-1
Unit cell dimensions (Å, °)	a = 11.0029(6)	a = 9.3823(5)
	b = 17.4560(10)	b = 9.6238(5)
	c = 12.2221(8)	c = 16.2075(9)
	β = 116.710(2)	α = 75.865(3)
		β = 84.750(2)
		γ = 86.911(2)
V(Å^3)	2097.0(2)	1412.41(13)
Z	4	2
Density (calc.) (Mg/m^3)	1.840	1.864
Absorption coefficient (mm^{-1})	5.955	4.812
F(0 0 0)	1128	772
θ range for data collection (°)	2.072–27.385	1.300–28.220
Index ranges	−14/14;	−8/12;
	−22/22;	−12/12;
	−15/8	−21/21
Reflections measured	18,242	28,980
Observed data [$I > 2\sigma(I)$]	4678	6944
Data/restraints/parameters	4678/4/255	6944/0/345
Goodness of fit on F^2	1.044	1.050
R, wR^2	0.0191, 0.0388	0.0237, 0.0419

Table 2
Selected experimental and optimized bond lengths [Å] and bond angles [°] of **3**.

	Experimental	Optimized
Re(1)-N(1)	2.244(2)	2.3386
Re(1)-O(1)	2.198(2)	2.2680
Re(1)-Cl(1)	2.4819(6)	2.5131
Re(1)-C(15)	1.901(2)	1.9021
Re(1)-C(16)	1.926(3)	1.9143
Re(1)-C(17)	1.910(2)	1.9105
N(2)-C(9)	1.433(3)	1.4264
N(2)-C(3)	1.374(3)	1.3745
N(3)-C(6)	1.375(3)	1.3891
O(1)-Re(1)-(N1)	80.03(7)	76.88
O(1)-Re(1)-C(15)	176.91(9)	174.14
N(1)-Re(1)-C(16)	171.19(9)	170.89
Cl(1)-Re(1)-C(17)	173.89(7)	172.05

Table 3
Selected experimental and optimized bond lengths [Å] and bond angles [°] of **4**.

	Experimental	Optimized
Re(1)-N(2)	2.254(2)	2.3032
Re(1)-O(1)	2.165(2)	2.2658
Re(1)-Cl(1)	2.4648(6)	2.5101
Re(1)-C(21)	1.914(3)	1.9188
Re(1)-C(22)	1.936(2)	1.9149
Re(1)-C(23)	1.893(3)	1.8956
N(2)-C(12)	1.304(3)	1.3018
C(12)-C(13)	1.429(3)	1.4280
C(13)-C(14)	1.341(3)	1.3543
N(6)-C(1)	1.437(3)	1.4247
N(5)-C(9)	1.354(3)	1.3921
N(6)-C(7)	1.355(3)	1.3674
O(1)-Re(1)-(N2)	78.57(6)	75.68
O(1)-Re(1)-C(23)	174.14(9)	175.66
N(2)-Re(1)-C(21)	169.6(1)	169.28
Cl(1)-Re(1)-C(22)	173.86(7)	174.39

2.9. Computational details

Gaussian 09 W was used to conduct the computational experiments [15]. Geometry optimizations of the rhenium complexes were achieved through DFT calculations using the B3LYP functional, with an accompanying hybrid basis set *viz.* the 6-311G^{++} (d, *p*) basis set was applied to all the C, H, N, O, and Cl atoms and the LANL2DZ basis set applied to the metal centre [16,17]. The crystal structures were used as starting structures with solvents of recrystallization removed prior to any calculations. Using the optimized structures of the metal complexes, frequency calculations confirmed that the respective structures are at global minima on the potential energy surfaces and from these, the vibrational energies were attained [18]. The close correlation between the optimized and geometrical parameters of compounds **3** and **4** is emphasized by the low calculated RMSD values (**3**: 0.0986 Å and **4**: 0.5700 Å) Fig. 3. The larger RMSD value of **4** is mainly attributed to the flexible degree of rotation of the C—C single bonds within its chelating ligand. The molecular docking simulations were conducted using Patchdock Beta version 1.3 and the different data sets were refined using Firedock [19]. All data processing was conducted with Yasara view [20]. The optimized conformers of the respective rhenium compounds were used as the small molecules while the water molecules of recrystallization were removed from the B-DNA crystal structure (LOX) (PDB ID: 1F8N) and the resultant conformer was used as the receptor.

2.10. UV-Vis DNA binding titrations

Calf thymus (CT)-DNA was prepared in phosphate-buffered saline (PBS) at a pH of 7.2 and the DNA binding studies of the metal complexes were carried out in MeOH. The DNA solution afforded a ratio of UV absorbance at 260 and 280 nm of approximately 1.9:1 which indicates that the DNA was sufficiently free of protein [21]. In addition, the CT-DNA concentration per nucleotide was determined by UV absorption spectroscopy using the molar absorption coefficient ($\varepsilon_{260} = 6600\ M^{-1}\ cm^{-1}$) [21]. The resultant stock DNA solution was stored at a temperature of 4 °C and used within 2 days after preparation. Prior to any additions of CT-DNA aliquots, separate methanolic standard solutions of **1**–**4** were monitored spectrophotometrically during various time intervals over 24 h to confirm the stabilities of the respective rhenium compounds in methanol. Afterwards, the respective metal complexes and CT-DNA solutions were incubated for 24 h at 25 °C prior to any UV-Vis measurements [22]. Furthermore, the UV-Vis spectra were attained for a solution of metal complex (of known concentration in methanol) with varying nucleotide concentrations (0–200 μM) in PBS. The data attained from the absorption titration experiments were fitted to the following equation to obtain the intrinsic binding constant (K_b):

$$[DNA]/(\epsilon_a - \epsilon_f) = [DNA]/(\epsilon_b - \epsilon_f) + 1/K_b(\epsilon_b - \epsilon_f)$$

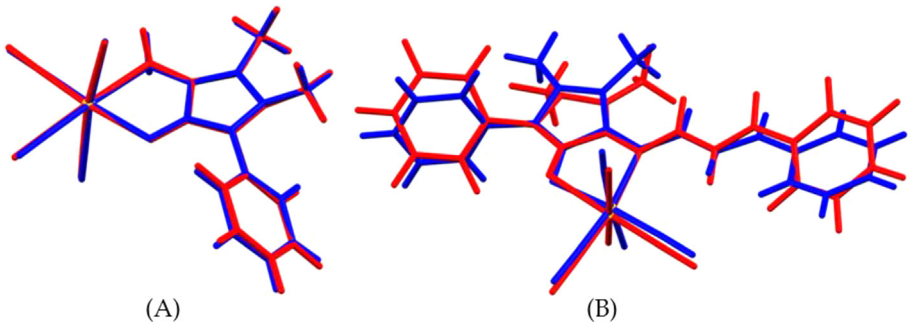

Fig. 3. Overlay structures of the optimized (red) and crystal structures (blue) for compounds **3** (A) and **4** (B). (For interpretation of the references to colour in this figure legend, the reader is referred to the web version of this article.)

In this equation, [DNA] is the concentration of DNA in base pairs, ε_a is the extinction coefficient of the observed absorption band at the given DNA concentration (corresponds to A_{obs}/[complex]), ε_f is the extinction coefficient of the complex free in solution, and ε_b is the extinction coefficient of the complex when fully bound to DNA. A plot of [DNA]/[$\varepsilon_a-\varepsilon_f$] versus [DNA] gave a slope 1/[$\varepsilon_a-\varepsilon_f$] and Y intercept equal to 1/K_b[$\varepsilon_b-\varepsilon_f$]. The intrinsic binding constant (K_b) is estimated to be the ratio of the slope to the intercept [22].

Gel electrophoresis experiments were conducted using a Bio-Rad Experion™ Automated Electrophoresis System which includes the Experion™ electrophoresis station with its accompanying peripheral devices, priming station and vortex station II. Data capturing and manipulation were achieved with the aid of the Experion software. A set of 2 mM CT-DNA solutions prepared *via* the same method as specified before were incubated with varying concentrations of the respective metal compounds for a period of 24 h. Utilizing the DNA 1 K Analysis Kit and the protocols applied to chip preparation, the respective samples were loaded and run on the instrument.

3. Results and discussion

3.1. Synthesis, characterization and computational studies

The formation of **1** and **2** is a typical illustration of template synthesis where condensation and coordination reactions occur in a complementary manner [23,24]. Characteristic to this class of synthetic approach, the isolation of the free Schiff bases, *viz.* ciap or cuap could not be achieved in sufficient purity. The bridging bidentate chelates of these dinuclear rhenium(I) compounds act as bidentate monoanionic moieties. In the case of the mononuclear rhenium(I) complexes **3** and **4**, the cumap Schiff base hydrolysed upon coordination leading to formation of the neutral bidentate coordination mode of $N_{amino}O_{ketone}$ for the 4-aminoantipyrine moiety (in **3**) whilst cinap remained intact and coordinated through its neutral $N_{imino}O_{ketone}$ donor pair (in **4**). The diverse coordination patterns of the cinap and cumap ligands were rationalized through DFT studies (see Table 4).

Although, the optimized structure of cinap has a higher computed total energy than cumap, ligand cinap has a lower calculated band-gap energy. In addition, the bond angle C_{apy}-N_{imino}-C_{imino} (where apy = aminoantipyrene moiety) of cinap is closer to the idealized bond angle of 120° for a bond containing a bridging imino nitrogen. More interestingly, the Natural Population Analysis (NPA) charges of the imino carbon and nitrogen atoms suggest that the isopropylbenzene moiety of cumap induces a stronger inductive effect as compared to the 1-ethenylbenzene moiety of cinap. This is further evident from visual inspection of the Electrostatic Potential (ESP) surfaces of the two Schiff base conformers whereby the ESP surface of cumap shows that its phenylimino moiety is approaching negative ESP values whereas the 1-((imino)ethenyl) benzene moiety of cinap generally exhibits ESP neutrality. This implies that the imino bond of cumap is weaker than that of cinap. Therefore, the main computational factor that rationalises the experimental instability of cumap is denoted to cumap's phenylimino moiety which generates a higher inductive influence as compared to the 1-((imino)ethenyl)benzene moiety of cinap. In turn, the experimental stability of cinap is mainly emphasized by its computed frontier orbitals which shows a more extended *pi*-delocalized system over its 1-((imino)ethenyl)benzene moiety; ultimately leading to its propensity not to undergo hydrolysis [25,26].

The low molar conductivity values of **1**–**4** (12.22–20.95 Ω^{-1} cm^{-2} mol^{-1}) affirm that the metal compounds exist as neutral molecules in solution. Additionally, these metal compounds display moderate solubility in alcohols and mid to high solubility in polar aprotic solvents. The low resolution X-ray structures for **1** and **2** are nearly identical whereby two geometrically equivalent imino moieties coordinate in a bidentate manner *via* N_{imino}, bridging $O_{phenolate}$ moieties. Consequently, the ^{1}H NMR spectra of these metal compounds essentially show non-distinguishable proton signals for their chelators due to chemical equivalence, see Figs. S3, S5, S7 and S9. The proton spectra for **1**–**4** show well resolved peaks, illustrating the diamagnetic nature of each metal compound. Imine signals are observed at 8.52 (doublet), 8.71 (singlet) and 7.82 ppm (doublet) for **1**, **2** and **4**, respectively. An upfield shift of the imine peak is noted between the free-ligand cinap (9.42 ppm) and its corresponding metal complex (**4**). A comparison between the free-ligand cumap and its metal complex (**3**) affirms that this Schiff base has cleaved given that the free-ligand's imino singlet at 9.57 ppm is not evident in the proton spectrum of **3**. A similar conclusion is drawn when comparing the IR spectra of **3** and its free-ligand, cumap, where N—H vibrational bands in the region of 3100 cm^{-1} are visible for the metal complex but not for the free-ligand. Mutual for all solid-state infrared spectra of the metal compounds are the high-intensity carbonyl stretches between 1872 and 2022 cm^{-1}, see Figs. S2, S4, S6 and S8. In addition, the aminoantipyrene ketonic bonds vibrate at cumap, cinap, **3** and **4** at 1654, 1637, 1608 and 1600 cm^{-1}, respectively, with the vibrational bands shifts between free ligands and their respective complexes affirming that coordination occurred. Additionally, medium to strong υ(C═N) and υ(C═C) stretches are common to **1** and **2** [between 1565 and 1684 cm^{-1}].

The electronic spectra for **1**–**4** display several absorption bands between 235 and 461 nm. The electronic transitions between 200 and 350 nm are ascribed as intraligand $\pi \rightarrow \pi*$ transitions while those above 350 nm are ascribed to metal-to-ligand charge transfer bands [27]. Common to most *facial* tricarbonylrhenium(I) compounds, no metal-based electronic transitions are observed due to their low-spin d^6-electronic configuration. *Facial* tricarbonylrhe-

Table 4
Summary of the computational data for cumap and cinap.

	Ligand cumap	Ligand cinap
Total Energy (eV)	-2.8681×10^4	-2.7565×10^4
NPA charge of N_{imino}	−0.473	−0.418
NPA charge of C_{imino}	0.121	0.106
Band-gap energy (eV)	4.04	3.40
Electrostatic potential surfaces	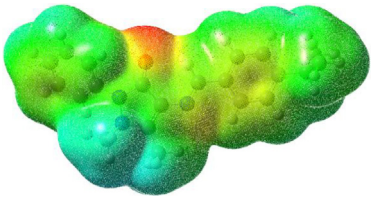	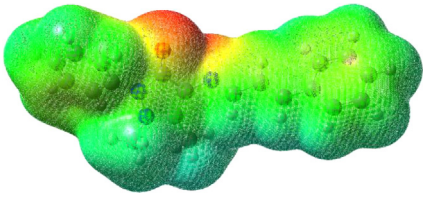
HOMO surfaces	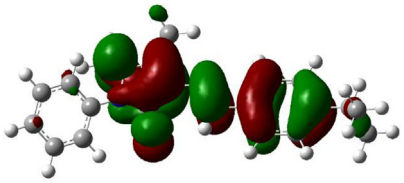	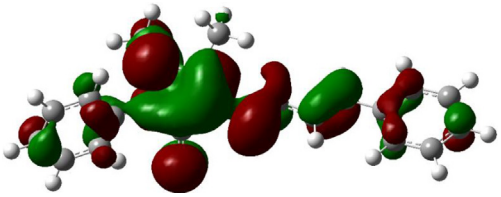
LUMO surfaces	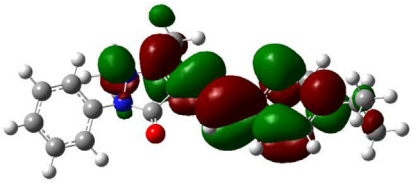	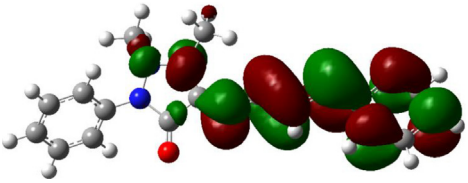
C_{apy}-N_{imino}-C_{imino} (°)	121.047	120.535

nium(I) compounds tend to exhibit the redox behaviour: Re(I) → Re(II) + e^- [28] and these irreversible processes are observed for **1**–**4** at E_{pa} = 0.96 V, 1.04 V, 1.09 V and 1.11 V, respectively Figs. S12–S16. The values are within range for literature reported rhenium(I) compounds: 0.83–1.60 V *vs* Ag|AgCl [29,30]. Further irreversible processes at E_{pa} = 0.68 V (for 1), E_{pa} = 0.58 V (for **2**), E_{pc} = 0.44 V (for **3**) and E_{pc} = 0.64 V (for **4**) are tentatively assigned as ligand induced redox processes. Additionally, the linearity of the figure insets [plots of I_{pa} (anodic peak current) *vs* $v^{1/2}$ (square root of scan rate)] confirm that the redox processes adhere to diffusion controlled behaviour.

3.2. Description of crystal structures 3.C_4H_8O and 4.2(CH_2Cl_2)

Compound **3** co-crystallizes with a tetrahydrofuran molecule of recrystallization in the space group $P2_{1/c}$ whereas **4** displays an inverted symmetry (*P*-1 space group) and is accompanied with two dichloromethane molecules of recrystallization Figs. 4 and 5. Both metal compounds are monomeric, neutral and the crystal lattice of **3**.C_4H_8O is stabilized by a series classical hydrogen bonding patterns. In fact, Cl1 H1A-N1 [2.3117 Å] intermolecular hydrogen-bond between neighbouring molecules of **3** allows them to pack in columns aligned with the [*c*]-axis, see Fig. S17. Ultimately this affords a polymeric network structure which is further supported by classical hydrogen bonding interactions between the other amino hydrogens and its solvent molecules [O5···H1B = 2.3117 Å]. In the case of **4**, typical *pi*-stacking interactions (below 3.5 Å) are observed between the C15-C20 phenyl ring and sp^2-hybridized C13 and C14 atoms with respective centroid to carbon distances of 3.458 and 3.383 Å. These interactions allow the molecules of **4** to afford *pi*-stacked columns parallel to [*b*]-axis and these columns are supported by non-classical hydrogen bonding with the bridging dichloromethane molecules.

The central cause for the deviation from perfect octahedral symmetry stems from 5-membered chelate rings which affords

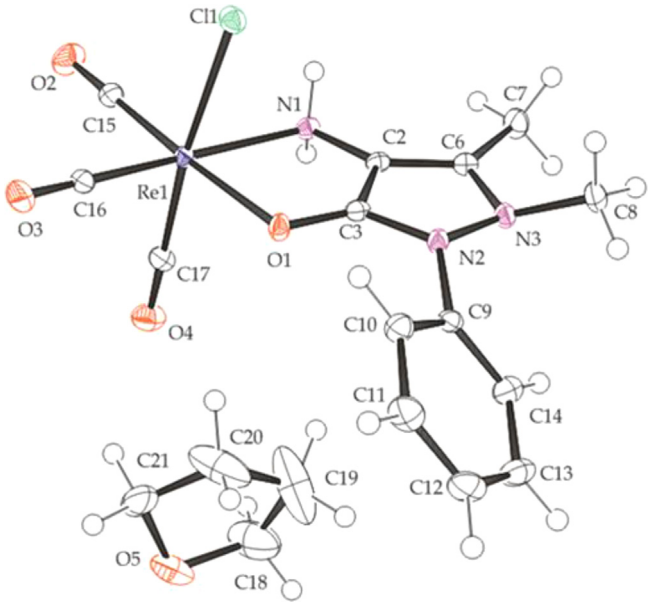

Fig. 4. ORTEP view of compound **3**·C_4H_8O showing 50% probability displacement ellipsoids and the atom labelling.

constrained bite angles for **3** and **4**, respectively: O1-Re1-N1 = 80.03(7)° and O1-Re1-N2 = 78.57(6)° which are substantially smaller than the expected bond angles of 90°. This distortion induces deviation from linearity for the O1-Re1-C15 [176.91(9)°], N1-Re1-C16 [171.09(9)°], Cl1-Re1-C17 [173.89(7)°] bond angles for **3** and O1-Re1-C23 [174.14(9)°], N2-Re1-C21 [169.6(1)°], Cl1-Re1-C22 [173.86(7)°] for **4**. The flexibility in the aliphatic N2-C12-C13-C14 moiety in **4** induces the C15-C20 phenyl ring to form a dihedral angle of 14.49° with respect to the C21C23N2O1 basal

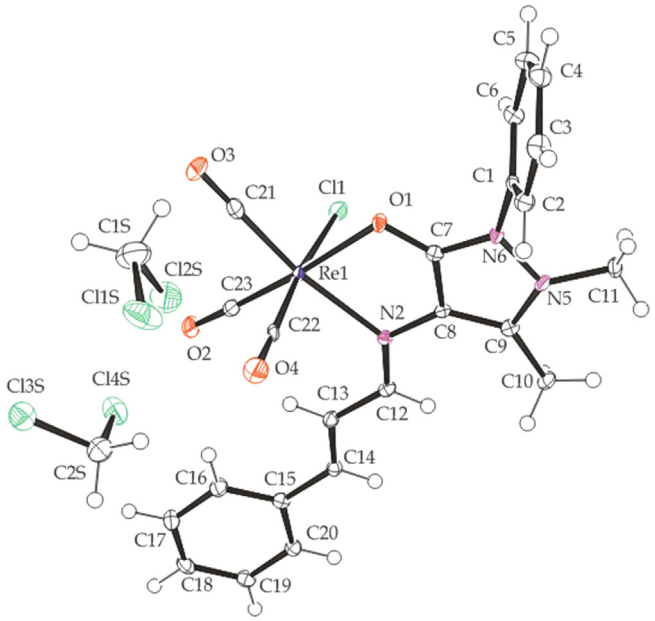

Fig. 5. ORTEP view of **4**.2 (CH_2Cl_2) showing 50% probability displacement ellipsoids and the atom labelling.

plane. The optimized conformer of **4** has similar bond distances for N2-C12 [1.304(3) Å for experimental and 1.3018 Å for optimized], C12-C13 [1.429(3)° Å for experimental and 1.4280 Å for optimized] and C13-C14 [1.341(3)° Å for experimental and 1.3543 Å for optimized] which supports the sp^2-hybridized nature of the atoms. A similar phenomenon was found in the optimized conformer of **3** where a plane-to-plane angle of 21.68° was found between the C21C23N2O1 basal plane and C15-C20 phenyl ring. The bond order of the N2-C9 (for **3**) and N6-C1 (for **4**) is clearly established based on their bond lengths and these single bonds [1.433(3) Å for **3** and 1.437(3) for **4**] allow wider dihedral angles [43.95 for **3** and 74.79° for **4**] between pyrazole and appending phenyl rings. The same also accounts for the Schiff base functionality in **4** [N2-C12 = 1.304(3) Å] which is shorter than the intracyclic pyrazole C—N bonds of **3** [N2-C3 = 1.374(3) Å and N3-C6 = 1.375(3) Å] and **4** [N5-C9 = 1.354(3) Å and N6-C7 = 1.355(3) Å].

Metal compounds **3** and **4** coordinate in a similar manner *via* ketonic oxygen atoms and nitrogen donors [amino (for **3**) or imino (for **4**)] donor atoms from their respective antipyrene moieties. In comparison to **3**, a similar coordination mode was observed for the rhenium(V) compound: *cis*-[$ReBr_2$(pap)(H_2pap)(PPh_3)](ReO_4) (H_2pap = 4-aminoantipyrene) where the 4-aminoantipyrene moiety acts a neutral bidentate chelator [31]. The Re-N_{amino} [**3**: 2.244 (2) Å] and Re-$O_{ketonic}$ [3: 2.198(2)] bond lengths for **3** are both slightly longer than the equivalent bonds of the cited rhenium(V) compound [2.19(1) and 2.102(9) Å] and is attributed to the less acidic nature of the *fac*-[$Re(CO)_3$]$^+$ core. The coordination bonds for **3** and **4** [**4**: Re-N_{imino} = 2.254(2) Å; **4**: Re-$O_{ketonic}$ = 2.165(2) Å] compare well with analogous tricarbonyl rhenium(I) bonds found in literature, Re-N_{amino}: 2.196(2) – 2.244(4) Å [32], Re-N_{imino}: 2.208(3)–2.258(4) Å [33,34] and Re-$O_{ketonic}$: 2.164(5)–2.195(2) Å [35,36]. Indicative to literature trends, the rhenium(I) carbonyl bonds [**3**: Re1-C15 = 1.901(2) Å, Re1-C16 = 1.926(3) Å, Re1-C17 = 1.910(2) Å and **4**: Re1-C21 = 1.914(3) Å, Re1-C22 = 1.936(2) Å, Re1-C23 = 1.893(3) Å] are different which is largely ascribed to the different degree of *trans*-influence imposed on their carbonyl co-ligands [30,37]. Furthermore, the rhenium(I) to chloride coordinative bonds, Re-Cl [**3**: 2.4819(6) Å, **4**: 2.4648(6) Å] are within the range of other reported axial Re-Cl bond lengths [2.452(4)–2.491 (2) Å] [38,39].

3.3. DNA interaction studies

3.3.1. UV-Vis DNA binding of *1–4*

Steady state absorption spectroscopy has been used to study the binding mode and the strength of the binding interaction between the rhenium(I) complexes and CT-DNA. An intercalating binding mode generally results in hypochromism coupled with a distinct red shift of the absorption band [40]. Upon the addition of CT-DNA, compounds **1**, **2** and **4** display 7–19% hyperchromism of their absorption maxima (**1**: 283 nm, **2**: 282 nm and **4**: 350 nm) with negligible red or blue shifts, implying a lack of significant structural contusions of the DNA Figs. 6–9. For **3**, a slight blue shift (261–258 nm) is seen upon the first CT-DNA aliquot addition, signifying an initial destabilization of the DNA helix [41] but thereafter, no further shifting is observed during hyperchromic steps. Isosbestic points are noted at 310 and 378 nm for **1** and 279 and 380 nm for **4**. Hence, the electronic spectral changes for **1–4** are consistent with metal complexes of a groove-binding nature [42–44]. Furthermore, the calculated K_b values [**1**: 8.48 (±0.42) x10^3 M^{-1}, **2**: 5.76 (±0.73) × 10^3 M^{-1}, **3**: 4.38 (±0.39) × 10^4 M^{-1}, **4**: 1.10 (±0.55) × 10^5 M^{-1}] are within literature range for other Schiff base containing, groove-binding metal complexes (10^3 M^{-1} > K_b > 10^6 M^{-1}) [45–48].

3.3.2. Molecular docking

Molecular docking simulations of **1–4** were conducted to further ascertain the compounds' modes of interactions to DNA. The most stable adducts of **1–4** with B-DNA affirm their groove-binding nature where all four compounds dock within the minor groove (base pair region: AT, GC, CG, GC, CG) Figs. 10–13. The large dinuclear structures of **1** and **2** (van der Waal's radii: 10.270 Å and 10.113 Å respectively) prevents manoeuvrability within B-DNA grooves and attests for their low intrinsic binding constants. The mononuclear compounds **3** and **4** (van der Waal's radii: 7.212 Å and 9.835 Å respectively) display similarity where the bidentate chelators interact with the hydrophobic B-DNA interior and the more polar carbonyl co-ligands situate towards the hydrophilic exterior. Compounds **3** and **4** are stabilized primarily by hydrogen bonding [**3**: antipyrene C_{methyl} atom with a guanine N atom (2.472 Å) and **4**: antipyrene C_{methyl} atom with a cytosine O_{ketone} atom (2.477 Å)]. Further close contacts are observed for **4** [Cl atom with an $O_{phosphate}$ atom (2.488 Å); axial $O_{carbonyl}$ with a carbon-phosphate backbone C atom (2.476 Å) and an alkyl C atom with a guanine N_{amine} atom (2.450 Å)]. This stronger bonding pattern for **4** results in a lower total global energy than that of **3** (**3**: −42.79 kJ.mol^{-1} and **4**: −52.34 kJ.mol^{-1}) and corroborates **4**'s higher intrinsic binding constant (K_b) quantified in the previous section.

3.3.3. Gel electrophoresis

The virtual gel stains of compounds **1** and **2** indicate that both compounds cleave CT-DNA best at lowest concentration (lanes 1 and 4) with **2** having a similar cleaving activity at 10 and 50 μM concentrations (lanes 4 and 5) Fig. 14. A similar scenario is observed for **3** and **4** Fig. 15 however, for **3** at lowest concentration (lane 1), the cleaving ability is far greater than that observed for compounds **1**, **2** and **4**. This is possibly due to a combination of its smaller size (less steric effects) and higher affinity for DNA than the dinuclear complexes **1** and **2** or alternatively, **3** is able to produce a higher concentration of DNA-damaging radical species than the other metal compounds at lower concentrations [46]. Further to this, a trend of decreasing cleaving activity is noted for all four Re(I) compounds with increasing concentration, possibly due to aggregation at elevated concentrations [47]. The difference observed in the lanes 7 representing the CT-DNA only, is ascribed to variable stirring rates employed when the commercially attained CT-DNA fibres were dissolved in PBS buffer.

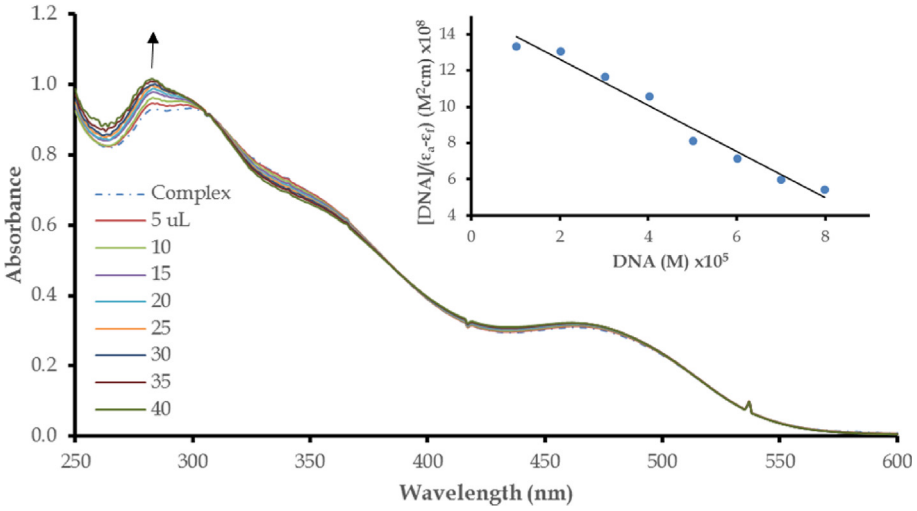

Fig. 6. The overlay UV–Vis absorption spectra of compound **1**. The dashed line indicates complex **1** free of any DNA and the hypochromic effect (indicated by the arrow) is due to progressive increments of a 5 mM CT-DNA solution.

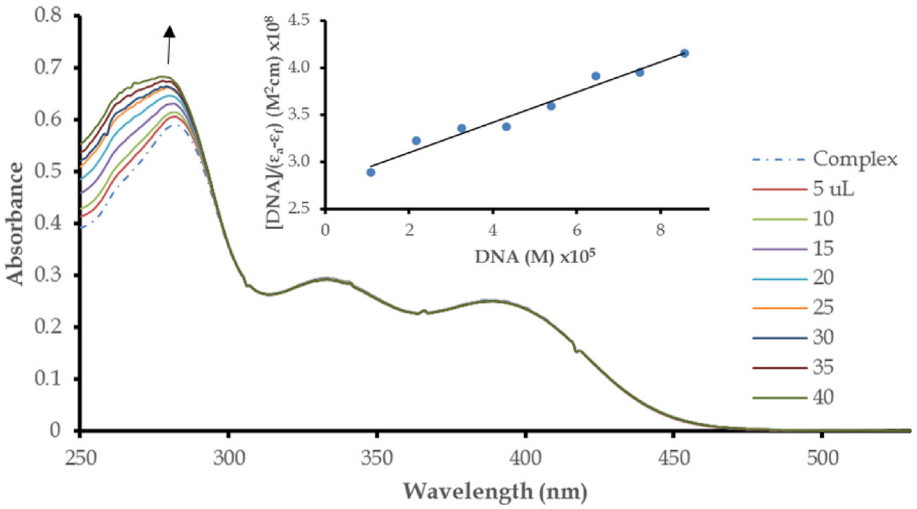

Fig. 7. The overlay UV–Vis absorption spectra of compound **2**. The dashed line indicates complex **1** free of any DNA and the hypochromic effect (indicated by the arrow) is due to progressive increments of a 5 mM CT-DNA solution.

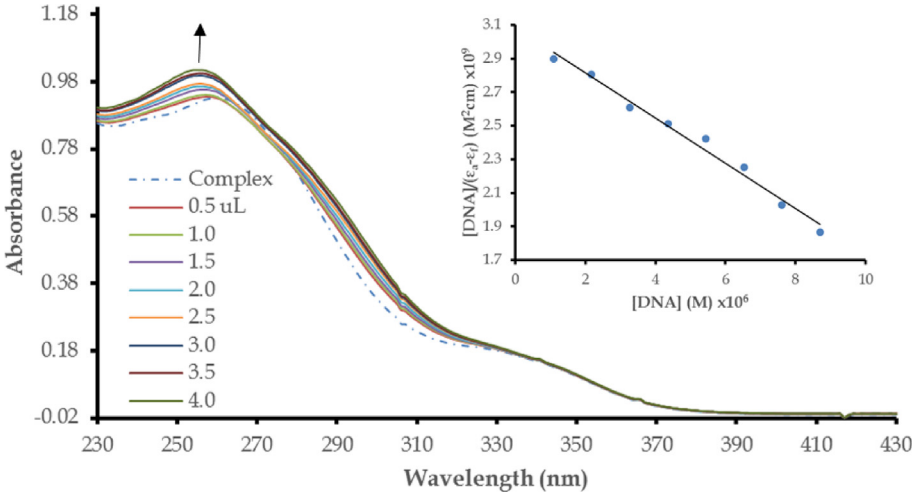

Fig. 8. The overlay UV–Vis absorption spectra of compound **3**. The dashed line indicates complex **1** free of any DNA and the hypochromic effect (indicated by the arrow) is due to progressive increments of a 5 mM CT-DNA solution.

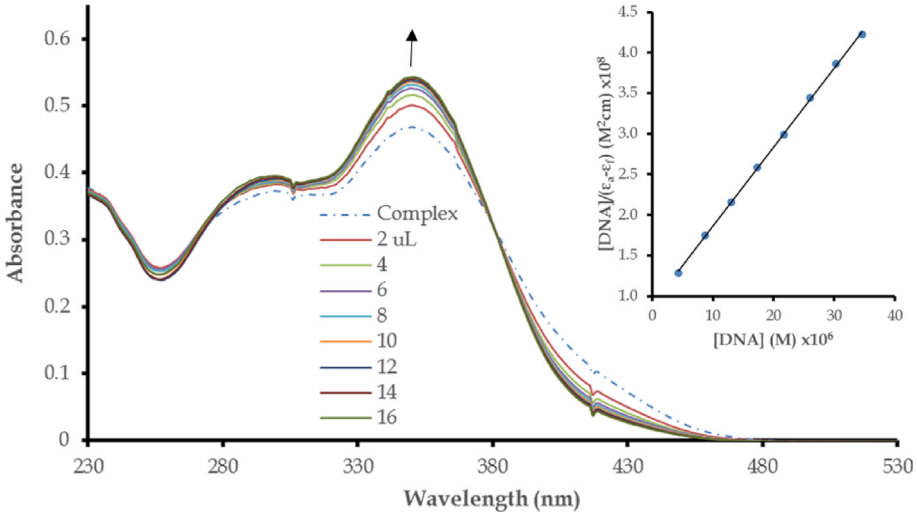

Fig. 9. The overlay UV–Vis absorption spectra of compound **4**. The dashed line indicates complex **1** free of any DNA and the hypochromic effect (indicated by the arrow) is due to progressive increments of a 5 mM CT-DNA solution.

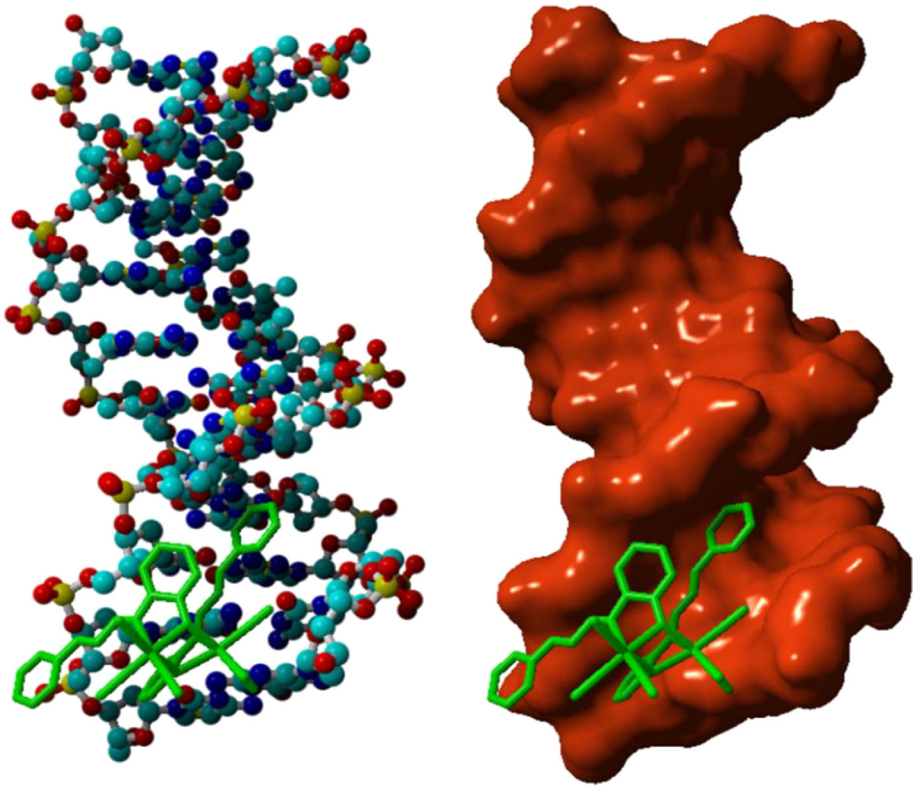

Fig. 10. Docked position of **1** bound to the minor groove of B-DNA: ball and stick view (left) and DNA molecular surface view (right).

4. Conclusion

The mono- and dinuclear *facial* tricarbonylrhenium(I) compounds **1**–**4** were formed and spectroscopically characterized. Structural elucidations of these metal compounds were confirmed by single crystal X-ray diffraction. The solid-state structure of **3** revealed that cumap underwent hydrolysis upon coordination to the rhenium(I) centre which ultimately led to the presence of the bidentate neutral 4-aminoantipyrine moiety in **3**. DFT studies suggested that the main computational factor that rationalises the experimental instability of cumap is ascribed to cumap's phenylimino moiety which generates a higher inductive influence as compared to the 1-((imino)ethenyl)benzene moiety of cinap. All the metal compounds were classed as DNA groove binders and their DNA interaction modes were supported by molecular docking simulations. Interestingly, the gel electrophoresis experiments showed that the metal compounds exhibit concentration dependant DNA cleavage activities.

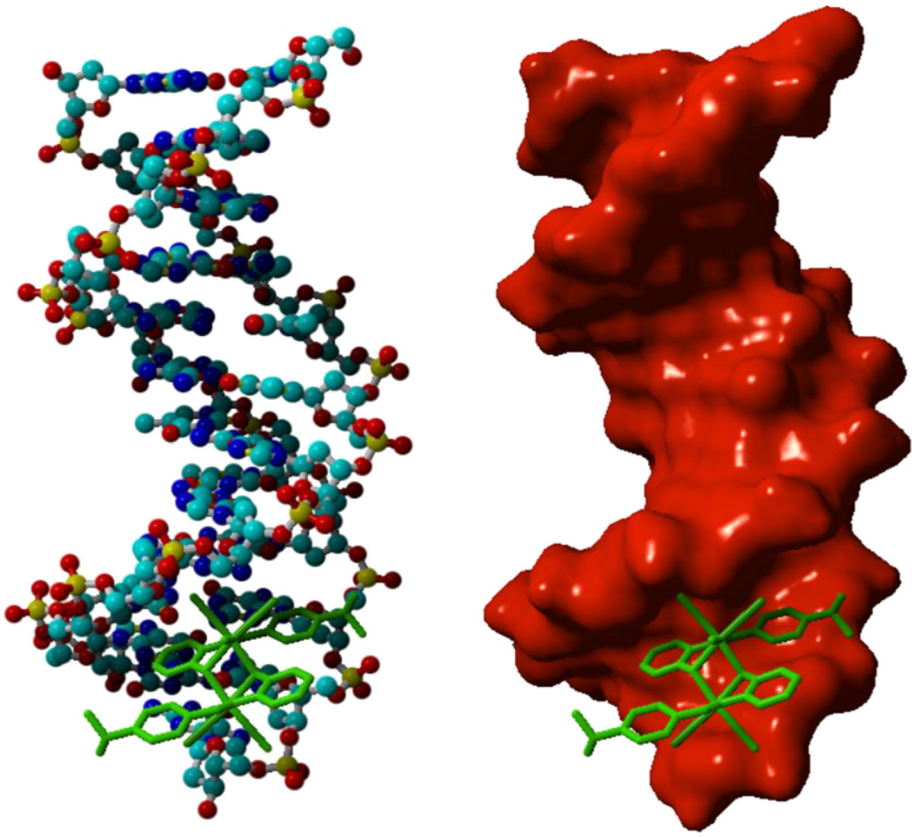

Fig. 11. Docked position of **2** bound to the minor groove of B-DNA: ball and stick view (left) and DNA molecular surface view (right).

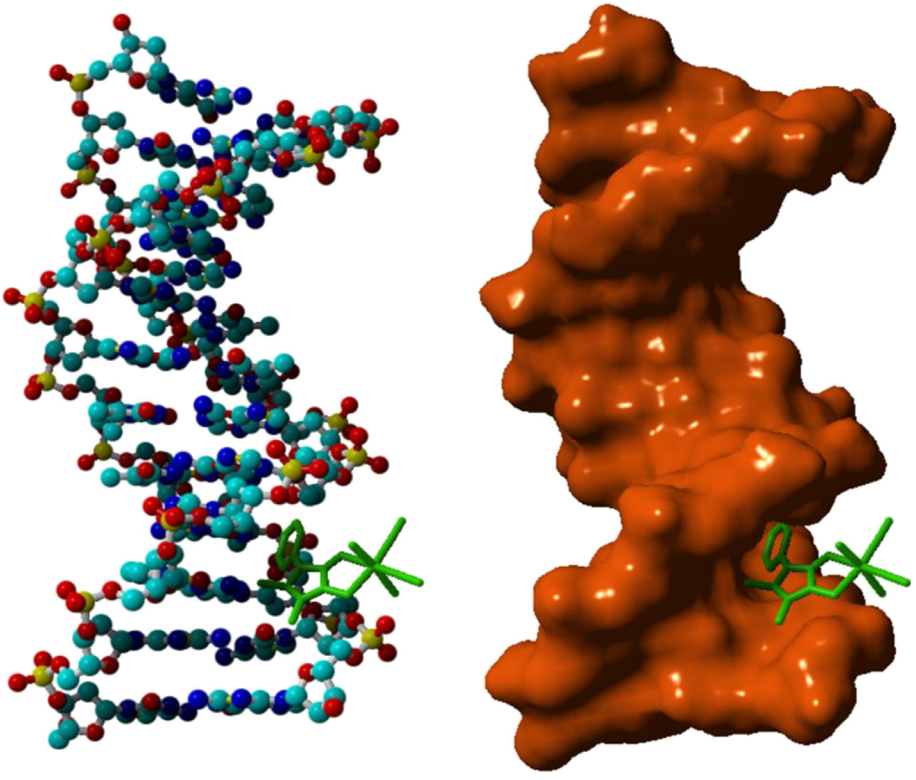

Fig. 12. Docked position of **3** bound to the minor groove of B-DNA: ball and stick view (left) and DNA molecular surface view (right).

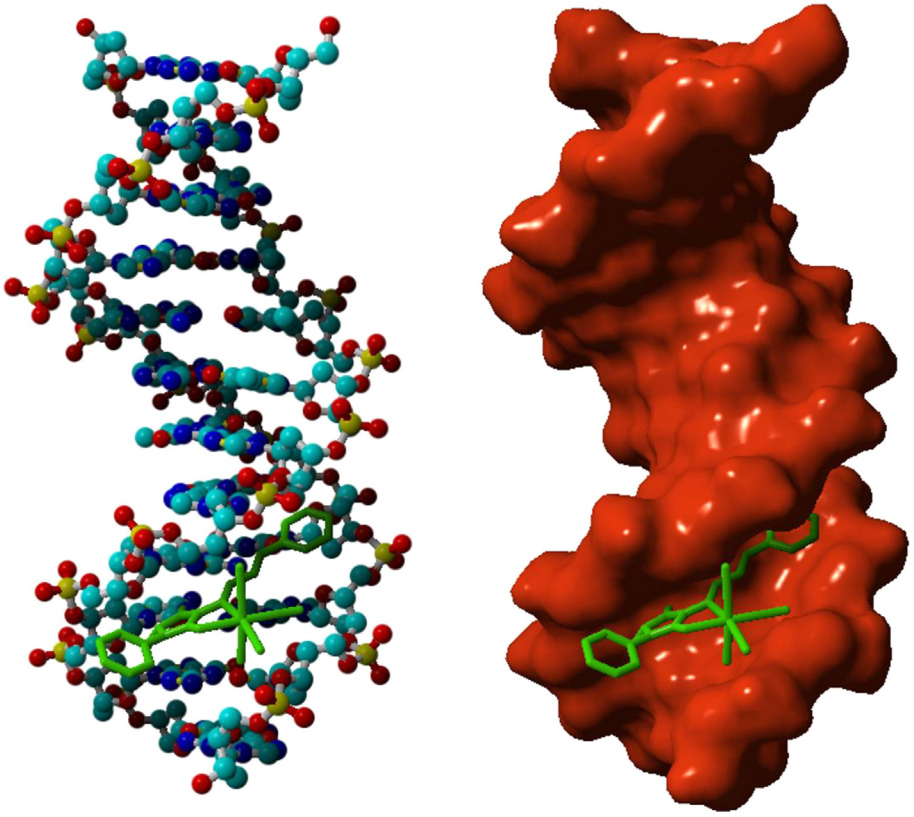

Fig. 13. Docked position of **4** bound to the minor groove of B-DNA: ball and stick view (left) and DNA molecular surface view (right).

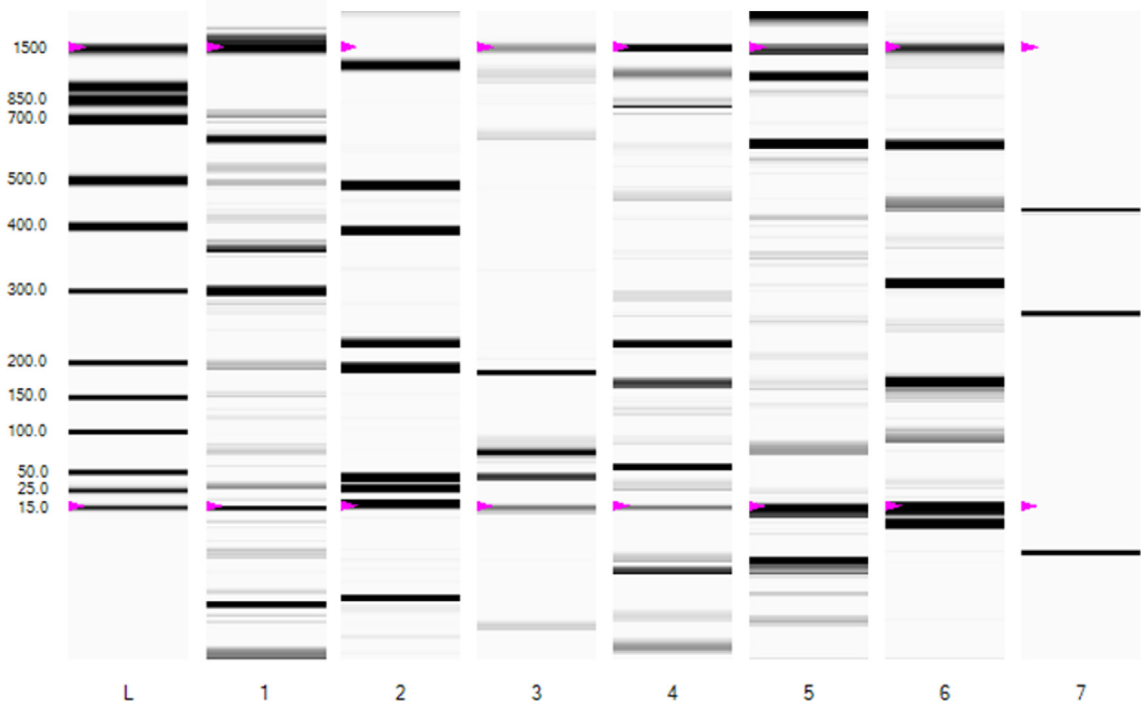

Fig. 14. Lane L: DNA Ladder of known base pair lengths, Lane 1: DNA + 10 μM of **1**, Lane 2: DNA + 50 μM of **1**, Lane 3: DNA + 100 μM of **1**; Lane 4: DNA + 10 μM of **2**, Lane 5: DNA + 50 μM of **2**, Lane 6: DNA + 100 μM of **2**; Lane 7: CT DNA only.

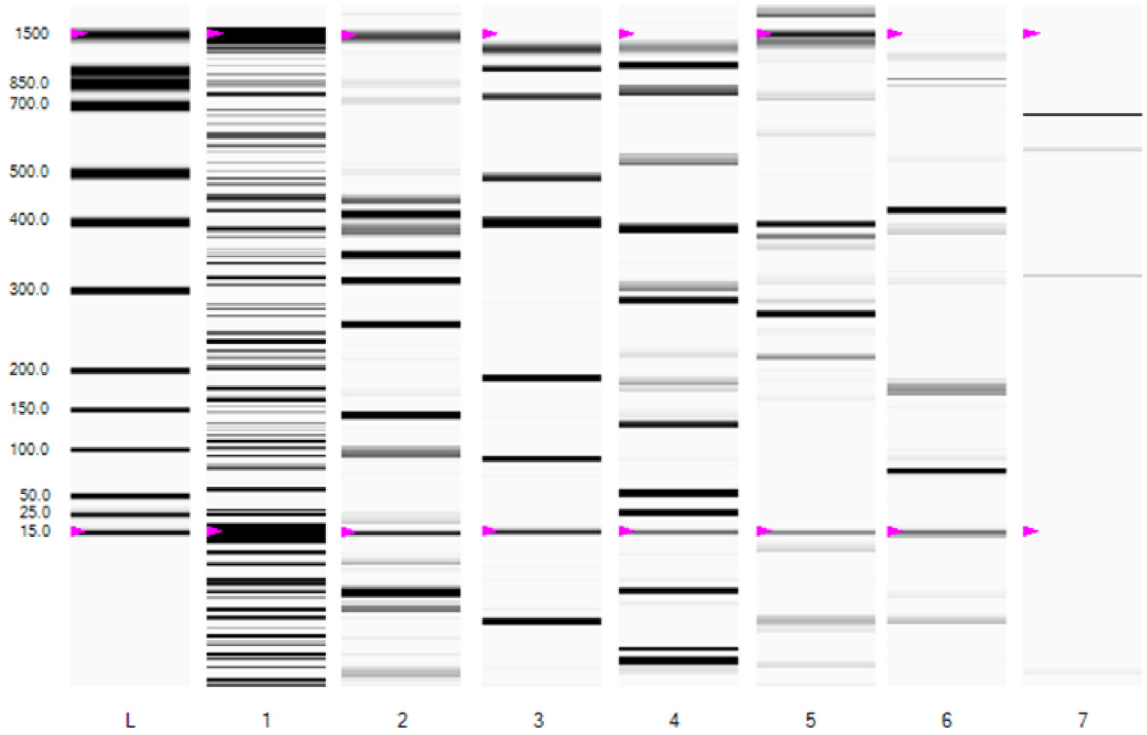

Fig. 15. Lane L: DNA Ladder of known base pair lengths, Lane 1: DNA + 10 μM of **3**, Lane 2: DNA + 50 μM of **3**, Lane 3: DNA + 100 μM of **3**; Lane 4: DNA + 10 μM of **4**, Lane 5: DNA + 50 μM of **4**, Lane 6: DNA + 100 μM of **4**; Lane 7: CT DNA only.

Acknowledgements

We are grateful to the University of KwaZulu-Natal, the National Research Foundation of South Africa and the Deutscher Akademischer Austauschdienst (DAAD) for financial support.

Appendix A. Supplementary data

CCDC 1817640 and 1817641contains the supplementary crystallographic data for this paper. These data can be obtained free of charge from The Cambridge Crystallographic Data Centre via www.ccdc.cam.ac.uk/data_request/cif. Supplementary data associated with this article can be found, in the online version, at https://doi.org/10.1016/j.ica.2018.03.032.

References

[1] F. Bakkali, S. Averbeck, D. Averbeck, M. Idaoma, Food Chem. Toxicol. 46 (2008) 446–475.
[2] T.J. Elizabeth, F. Gassara, A.P. Kouassi, S.K. Brar, K. Belkacemi, Crit Rev. Food. Sci. Nutr. 57 (2017) 1078–1088.
[3] S.F. Vaughn, G.F. Spencer, Am. Potato. J. 70 (1993) 527–533.
[4] A. Iyer, S. Panchal, H. Poudyal, L. Brown, Indian J. Biochem. Biophys. 46 (2009) 467–481.
[5] I. Kubo, I. Kinst-Hori, J. Agric Food Chem. 47 (1999) 4574–4578.
[6] J.S. Muhammad, S.F. Zaidi, S. Shaharyar, A. Refaat, K. Usmanghani, I. Saiki, T. Sugiyama, Biol. Pharm Bull. 38 (2015) 109–115.
[7] H. Ka, H.J. Park, H.J. Jung, J.W. Choi, K.S. Cho, J. Ha, K.T. Lee, Cancer Lett 196 (2003) 143–152.
[8] E.E. Mohamed, J. Pharmacol. Clin. Res. 2 (2017) 555585.
[9] S. Shreaz, R.A. Sheikh, R. Bhatia, K. Neelofar, S. Imran, A.A. Hashmi, N. Manzoor, S.F. Basir, L.A. Khan, Biometals 24 (2011) 923–933.
[10] F. Bisceglie, S. Pinelli, R. Alinovi, M. Goldoni, A. Mutti, A. Camerini, L. Piola, P. Tarasconi, G. Pelosi, J. Inorg. Biochem. 140 (2014) 111–125.
[11] Bruker APEX2, SAINT and SADABS. Bruker AXS Inc,, Madison, Wisconsin, USA, 2010.
[12] R.H. Blessing, Acta Cryst. A51 (1995) 33–38.
[13] G.M. Sheldrick, Acta Cryst. A64 (2008) 112–122.
[14] L.J. Farrugia, J. Appl. Cryst. 45 (2012) 849–854.
[15] M.J. Frisch, G.W. Trucks, H.B. Schlegel, G.E. Scuseria, M.A. Robb, J.R. Cheeseman, G. Scalmani, V. Barone, B. Mennucci, G.A. Petersson, H. Nakatsuji, M. Caricato, X. Li, H.P. Hratchian, A.F. Izmaylov, J. Bloino, G. Zheng, J.L. Sonnenberg, M. Hada, M. Ehara, K. Toyota, R. Fukuda, J. Hasegawa, M. Ishida, T. Nakajima, Y. Honda, O. Kitao, H. Nakai, T. Vreven, J.A. Montgomery Jr, J.E. Peralta, F. Ogliaro, M. Bearpark, J.J. Heyd, E. Brothers, K.N. Kudin, V.N. Staroverov, R. Kobayashi, J. Normand, K. Raghavachari, A. Rendell, J.C. Burant, S.S. Iyengar, J. Tomasi, M. Cossi, N. Rega, J.M. Millam, M. Klene, J.E. Knox, J.B. Cross, V. Bakken, C. Adamo, J. Jaramillo, R. Gomperts, R.E. Stratmann, O. Yazyev, A.J. Austin, R. Cammi, C. Pomelli, J.W. Ochterski, R.L. Martin, K. Morokuma, V.G. Zakrzewski, G.A. Voth, P. Salvador, J.J. Dannenberg, S. Dapprich, A.D. Daniels, O. Farkas, J.B. Foresman, J.V. Ortiz, J. Cioslowski, D.J. Fox, Gaussian 09 (Revision A.01),, Gaussian Inc, Wallingford, CT, 2009.
[16] A. Brink, H. Visser, A. Roodt, Polyhedron 52 (2013) 416–423.
[17] B. Machura, R. Kruszynski, Polyhedron 26 (2007) 3686–3694.
[18] K.C. Potgieter, T.I.A. Gerber, R. Betz, L. Rhyman, P. Ramasami, Polyhedron 59 (2013) 91–100.
[19] D. Duhovny, R. Nussinov, Wolfson HJ (2002) International Workshop on Algorithms in Bioinformatics (WABI 2002): Algorithms in Bioinformatics: 185–200; Schneidman-Duhovny D, Inbar Y, Nussinov R, Wolfson HJ, Nucl. Acids Res. 33 (2005) W363–W367.
[20] E. Krieger, G.J. Vriend, Comput. Chem. 36 (2015) 996–1007.
[21] M. Shakir, S. Khanam, M. Azam, M. Aatif, F. Firdaus, J. Coord. Chem. 64 (2011) 3158–3168.
[22] P. Mukherjee, O. Sengupta, M.G.B. Drew, A. Ghosh, Inorg. Chim. Acta 362 (2009) 3285–3291.
[23] G.F. Caramori, R.L.T. Parreira, A.M.D.C. Ferreira, Int. J. Quantum Chem. 112 (2012) 625–646.
[24] M. Ozdemir, M. Sonmez, F. Sen, M. Dincer, N. Ozdemir, J. Mol. Struct. 1127 (2017) 626–635.
[25] S. Van Wallendael, R.J. Shaver, D.P. Rillema, B.J. Yoblinski, M. Stathis, T.F. Guarr, Inorg. Chem. 29 (1990) 1761–1767.
[26] A.B.P. Lever, Inorg. Chem. 30 (1991) 1980–1985.
[27] E.R. Arce, I. Machado, B. Rodríguez, M. Lapier, M.C. Zúñiga, J.D. Maya, C.O. Azar, L. Otero, D. Gambino, J. Inorg. Biochem. 170 (2017) 125–133.
[28] R. Díaz, A. Francois, A.M. Leiva, B. Loeb, E. Norambuena, M. Yañez, Helv. Chim. Acta 89 (2006) 1220–1230.
[29] P. Mayer, E. Hosten, K.C. Potgieter, T.I.A. Gerber, J. Chem. Crystallogr. 40 (2010) 1146–1149.
[30] B. Machura, M. Wolff, I. Gryca, A. Palion, K. Michalik, Polyhedron 30 (2011) 2275–2285.
[31] S.B. Jiménez-Pulido, N.A. Illán-Cabeza, F. Hueso-Ureña, C.R. Maldonado, P. Sánchez-Sánchez, M.P. Fernández-Liencres, M. Fernández-Gómez, M.N. Moreno-Carretero, Dalton Trans. 45 (2016) 15142–15154.
[32] A.J. Graham, D. Akrigg, B. Sheldrick, Cryst. Struct. Commun. 6 (1977) 577–582.

[33] B. Machura, A. Świtlicka, M. Wolff, D. Tabak, R. Musioł, J. Polański, R. Kruszynskic, J. Organomet. Chem. 696 (2011) 731–738.
[34] P. Braunstein, L. Douce, F. Balegroune, D. Grandjean, D. Bayeul, Y. Dusausoy, P. Zanello, New J. Chem. 16 (1992) 925–929.
[35] V. Mirkhani, R. Kia, A.R. Vartooni, H.K. Fun, Polyhedron 29 (2010) 1600–1606.
[36] K.C. Potgieter, P. Mayer, T. Gerber, N. Yumata, E. Hosten, I. Booysen, R. Betz, M. Ismail, B. van Brecht, Polyhedron 49 (2013) 67–73.
[37] B.J. Coe, X.P. Foxon, R.A. Pilkington, S. Sánchez, D. Whittaker, K. Clays, N. Van Steerteghem, B.S. Brunschwig, Organometallics 35 (2016) 3014–3024.
[38] F.L. Thorp-Greenwood, M.P. Coogan, L. Mishra, N. Kumari, G. Rai, S. Saripella, New J. Chem. 36 (2012) 64–72.
[39] A. Zianna, G. Psomas, A. Hatzidimitriou, M. Lalia-Kantouri, RSC Adv. 5 (2015) 37495–37511.
[40] R. Eshkourfu, B. Čobeljić, M. Vujčić, I. Turel, A. Pevec, K. Sepčić, M. Zec, S. Radulović, T. Srdić-Radić, D. Mitić, K. Andjelković, D. Sladić, J. Inorg. Biochem. 105 (2011) 1196–1203.
[41] N. Sohrabi, N. Rasouli, M. Kamkar, Bull. Korean Chem. Soc. 35 (2014) 2523–2528.
[42] M. Vujčić, M. Lazić, M. Milenković, D. Sladić, S. Radulović, N. Filipović, K. Anđelković, J. Biochem. Mol. Toxicol. 25 (2011) 175–182.
[43] G. Barone, N. Gambino, A. Ruggirello, A. Silvestri, A. Terenzi, V.T. Liveri, J. Inorg. Biochem. 103 (2009) 731–737.
[44] A. Silvestri, G. Barone, G. Ruisi, D. Anselmo, S. Riela, V.T. Liveri, J. Inorg. Biochem. 101 (2007) 841–848.
[45] N.H. Khan, N. Pandya, K.J. Prathap, R.I. Kureshy, S.H.R. Abdi, S. Mishra, H.C. Bajaj, Spectrochim. Acta A 81 (2011) 199–208.
[46] G.S. Kurdekar, S.M. Puttanagouda, N.V. Kulkarni, S. Budagumpi, V.K. Revankar, Med. Chem. Res. 20 (2011) 421–429.
[47] M. Kaplanis, G. Stamatakis, V.D. Papakonstantinou, M. Paravatou-Petsotas, C.A. Demopoulos, C.A. Mitsopoulou, J. Inorg. Biochem. 135 (2014) 1–9.
[48] Q. Hua, R.Q. He, Protein Pept. Lett. 9 (2002) 349–357.